

Optimization of high-performance monocentric lenses

Igor Stamenov,* Ilya Agurok, and Joseph E. Ford

Department of Electrical and Computer Engineering, University of California San Diego,
9500 Gilman Drive, La Jolla, California 92093-0409, USA

*Corresponding author: istameno@ucsd.edu

Received 23 September 2013; accepted 15 October 2013;
posted 28 October 2013 (Doc. ID 198070); published 25 November 2013

The recent application of monocentric lenses for panoramic high-resolution digital imagers raises the question of the achievable performance limits of this lens structure and of techniques for design optimization to approach these limits. This paper defines the important regions of the design space of moderate complexity monocentric lenses and describes systematic and global optimization algorithms for the design of monocentric objective lenses of various focal lengths, apertures, and spectral bandwidths. We demonstrate the trade-off between spectral band, F-number and lens complexity, and provide design examples of monocentric lenses for specific applications. © 2013 Optical Society of America

OCIS codes: (080.3620) Lens system design; (110.0110) Imaging systems; (220.4830) Systems design.

<http://dx.doi.org/10.1364/AO.52.008287>

1. Introduction

Monocentric imaging lenses, which are constrained to have only spherical surfaces centered on a single point of symmetry, can produce a high-resolution image on a spherical image surface. Since high-resolution spherical detectors are not currently available, in practical application this image surface is optically transferred onto multiple conventional focal planes. This can be done by relay through multiple adjacent sets of secondary optics, as in monocentric multiscale imagers [1–3]. Alternately, it can be done via imaging fiber bundles with curved input and flat output faces, as in the monocentric fiber-coupled imagers [4–9]. These successful demonstrations motivate a more systematic exploration of the capabilities of the monocentric imaging lens.

In a lens with centered spherical or hemispherical surfaces, off-axis aberrations of coma and astigmatism are cancelled [10], but we need to correct spherical and chromatic aberration and their combination spherochromatism. Reducing spherochromatism is difficult, especially with large apertures. But despite

the monocentric constraint, and even with a small number of degrees of freedom, it is possible to obtain a number of useful designs [3,4,8,11].

In a previous paper [8], we reported the general aberration analysis of two-glass symmetric (2GS) monocentric lenses and results of our 2GS global search algorithm applied for a specific example, a 12 mm focal length, F/1.7, 120° field of view lens operating in 470–650 nm visible waveband. The algorithm described identified the optimum diffraction limited design [Fig. 1(a)] and a number of additional families of high-performing solutions. However, if we substantially increase the lens spectrum, light collection, or the scale, even after repeated 2GS global search, we will not achieve desired performance [Figs. 1(b)–1(d)]. The 2GS monocentric architecture reaches its limits.

Achieving a similar level of performance with these extended operating specifications demands more complex monocentric lens architectures, with more degrees of freedom. This is especially true when increasing more than one of these performance metrics. In this paper, we show methods and algorithms for advanced monocentric lens design. We categorize the monocentric lens design space, provide procedures for optimum and near-optimum lens design

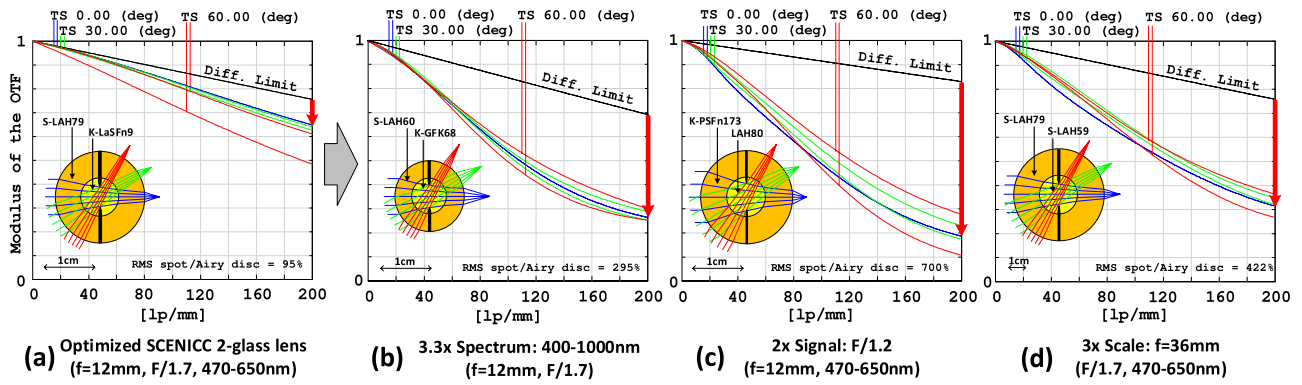


Fig. 1. MTF performance curves showing the limits of the globally optimized 2GS monocentric geometries. The examples are derived from an initial high-performing lens (a), which is pushed to improve spectral bandwidth (b), numerical aperture (c), or focal length (d) [using a 3× scale change to the illustration]. For each, the resolution of the two-glass structure drops well below the diffraction limit, indicating a need for greater complexity.

with complexity and performance trade-off considerations, and in Section 5 provide specific lens designs for selected applications.

2. Options for Improving Monocentric Lenses

A. Review of Monocentric Lens Architectures

The simplest monocentric lens architecture is a simple glass ball [12,13] with inset aperture stop. Historically, the more common approach was an achromatic 2GS architecture, used by Sutton in 1856, Baker in 1942 [14], and more recently by Brady and co-workers [1,3] and Ford and co-workers [2,15]. A more complex three-glass symmetric structure (3GS) with third-order aberration analysis was designed and fabricated by Oakley [16] for a panoramic spherical retroreflector. However, high order aberrations at large apertures were not systematically corrected.

Our goal was to push the performance of the existing lens and identify the limit of what monocentric lenses can or cannot do. We started by using commercial lens design software to explore the monocentric lens design space by a systematic increase of degrees of freedom in the system, while maintaining the monocentricity constraint, to identify the major configurations, which showed the most promise. We constrained the focal length and did a lens optimization for all options with a given number of degrees of freedom (i.e., glass choice, surface radius) and compared performance to the diffraction limit. Glass as an optical material has at least two description parameters, the index of refraction, and the Abbe number. To model the dispersion over a broader spectral range would require an expression with even more free parameters. But since we don't have the ability to create a glass with arbitrary index and dispersion, the choice of an existing glass material represents only a single degree of freedom. We use their accurate models described by Sellmeier, Extended, or Schott glass model formulas.

Figure 2 summarizes the result, showing 100 different geometries and the seven preferred design

architectures (drawn with a larger scale). Those preferred architectures were labeled as

- 1GS: One-glass symmetric with 1 degree of freedom (DOF)
- 2GS: Two-glass symmetric with 3 DOF
- 3GS: Three-glass symmetric with 5 DOF
- 3GA-7: Three-glass asymmetric with air gap and 7 DOF
- 4GA-8: Four-glass asymmetric with air gap and 8 DOF
- 4GA-9: Four-glass asymmetric with air gap and 9 DOF
- 5GA-10: Five-glass asymmetric with air gap and 10 DOF.

The 1GS, 2GS, 3GS, and 4GA-8 geometries were chosen for rigorous analysis and investigation, because they offered the best performance for their structural complexity.

The simplest 1GS geometry is a symmetric glass ball, with only one degree of freedom (1 DOF). When

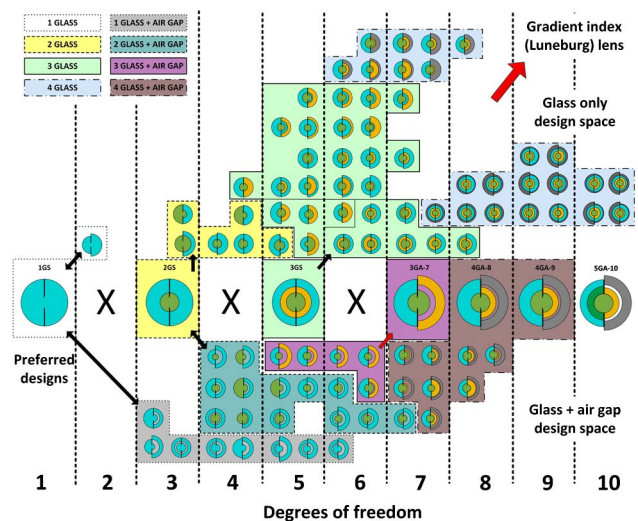


Fig. 2. Monocentric lens design space showing glass only (upper half) and glass with air gap (lower half) regions divided by the seven preferred design architectures in between.

the desired monocentric system is being designed, focal-length input constrains one of the radii, so the choice of glass in this structure remains as the single variable. Since there is no chromatism correction, this architecture is suitable mostly for monochromatic imagers with a relatively large F-number. In air, if we allow this geometry to become asymmetric, or increase degrees of freedom to two, the optimizer will converge back to the original 1GS structure as depicted in the upper half of Fig. 2. A similar outcome results if we introduce an air gap and push up to the maximum of six degrees of freedom (lower part of Fig. 2).

The next logical step was to make the achromatic lens with an additional glass, which yields the 2GS geometry with three degrees of freedom. As in 1GS geometry, optimization after lens splitting and introducing an air gap will converge back to the simpler 2GS geometry, while taking the upper “glass modification only” path on the chart by allowing all radii to vary will land in a 5DOF two-glass architecture that performs substantially the same as the simplest 2GS structure.

Adding the third and fourth glass in the monocentric structure and breaking the symmetry goes deep into the upper “glass modification only” region of the design space and offers only marginal improvement over 2GS and 3GS structures, not justifying the cost of manufacture. Therefore, simple symmetry breaking and glass adding is not productive. The upper half of the diagram is only partially populated—if we allow more glasses and more degrees of freedom, architecture will essentially converge to some variant of the Luneburg lens solution [17].

On the other hand, starting from 5DOF structure with three glasses and introducing an air gap also doesn't appear to help, as we continue along the lower part of Fig. 2 (glass with air gap path) up to the 6th degree of freedom. Then just a simple step over to the 7 degrees of freedom 3GA-7 architecture gives a substantial increase in performance, as shown with red arrow in Fig. 2. Further derivatives 4GA-8, 4GA-9, and 5GA-10 just keep up with the same trend. Out of these asymmetric structures with an air gap, 4GA-8 is the most attractive one to pursue with an addition of 5GA-10 for larger scale lenses where the maximum glass slab size plays an important role.

Looking at this comprehensive monocentric lens design space chart, an interesting fact is that simply adding the degrees of freedom at some point does not help. This is somewhat counter-intuitive. For the two, four, and six degrees of freedom cases, no preferred monocentric lens structure exists. All symmetry breaking attempts in this ≤ 6 DOF area inevitably converge back to the symmetric structures when the lens is designed for the use in air. A slight change to this rule applies only when the lens has a different medium in object and image space (e.g., an immersed lens), where a 4 DOF two-glass structure with symmetric core becomes the preferred design.

Our next goal was to find specific high-performance designs. To do this we developed global search algorithms for symmetric geometries, and systematic search methods for the asymmetric geometries with an air gap, as described in the following.

B. Review of Monocentric Lens Design Methods

Throughout the exploration of monocentric lens design space, several methods and optimization algorithms were developed. In previous work [8], we presented a global optimization algorithm for the 2GS architecture. Now a similar approach was used in one-glass (1GS) and three-glass (3GS) symmetric architectures, and a similar global search algorithm was developed. Since all these global optimization routines are essentially brute force calculations (for all possible glass combinations), with further increase in the number of degrees of freedom the cost of computing became prohibitive. Therefore, we developed systematic search methods. All the methods use spectral band, focal length, and F-number as an input for the desired system, and a predefined pool of commercially available glasses. These included the Schott, Ohara, Hoya, Sumita catalogs as well as CAF2 and fused silica, totaling 604 different materials available as of April 2013. Hikari, CDGM, and NHG manufacturers were not used because almost all of their glasses represent duplicate replacements of the glasses already included.

The optimization methods used, in order of increasing complexity and computation time, were

- 1GS global optimization algorithm (seconds to complete)
- 2GS global optimization algorithm (minutes to complete)
- 3GS global optimization algorithm (days to complete)
- 2GS seeded Hammer search (hours to days)
- 4GA-8 architecture 5-D “near global” search (up to 3 weeks).

Preliminary results of these methods were presented in [18] but will be described in more detail here. Global optimization algorithms for 1GS, 2GS, and 3GS architectures are multithreaded exact ray trace routines implemented in MATLAB. These check all possible glass choices (604 for 1GS, 364,816 for 2GS, and more than 220 million combinations for 3GS geometry). They were executed on PC workstations with two Intel 3.1 GHz Xeon E5-2687 W or four Intel 2.7 GHz Xeon E5-4650 Sandy Bridge based processors (16/32 CPU cores systems). The 3GS global optimization algorithm was also rewritten and tested on Kepler based NVIDIA K20 Tesla and K5000 Quadro GPU cards, with speed improvements on the order of 70 \times , effectively cutting down the computing time required from days to hours.

The 2GS seeded Hammer search approach used glass combinations of the top 2GS candidates obtained through global search, then imported in

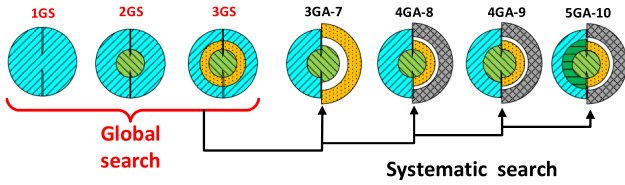


Fig. 3. Optimization of preferred monocentric lens geometries.

ZEMAX. The lens symmetry was broken and an air gap manually introduced.

Additional glass layers were added one by one, as shown in Fig. 3, with optimization at each step. In practice, the 2GS geometry was optimized by human assistance through ZEMAX Hammer search to 3GA-7 and then to 4GA-8 architecture or even more complex ones, if needed. The most complicated design approach, which was guaranteed to give the best result for the 4GA-8 geometry, was a five-dimensional “near global” search algorithm, also implemented in MATLAB. Like the seeded Hammer search, the 5D optimization algorithm starts with the core identified as the best 2GS candidates, and then the algorithm tries all combinations for the additional three glasses used in the 4GA-8 geometry. Because of five-dimensional optimization space complexity, this algorithm requires up to 3 weeks to complete running continuously on the 32CPU core workstation. We used this algorithm at the end of the lens design procedure to determine the absolute best candidate for manufacture and test.

3. Advanced Design Algorithms and Results

A. Improved 2GS Global Search Using 5 Wavelengths

In the previous paper [8] we reported a general aberration analysis of 2GS monocentric lenses, and applied a global search algorithm to identify the best design for a visible waveband monocentric lens. To generate a ranked list of all lens candidates, this algorithm used a three-step optimization for each possible two-glass combination: minimization of third-order Seidel spherical and longitudinal chromatism aberrations, exact ray trace for multiple ray heights at the central wavelength, and the calculation of polychromatic mean square wavefront deformation. The algorithm described was sufficiently accurate for the visible (photographic) spectral range, where the glass dispersion curve is approximately linear.

However, to look for solutions in an extended waveband, we modified the existing 3λ algorithm by replacing the first two steps by exact ray trace with five equally spaced wavelengths over the desired spectrum. The modified exact ray trace cost function became

$$Q = \sum_{m=1}^5 \left\{ \sum_{i=1}^3 \text{Abs}(\Delta S(h_i, \lambda_m)) + \sum_{j=1}^3 \sum_{k \neq j} \text{Abs}[\Delta S(h_j, \lambda_m) - \Delta S(h_k, \lambda_m)] \right\}, \quad (1)$$

where ΔS is longitudinal aberration of the ray of height h_i . Also, we modified the polychromatic mean square wavefront deformation calculation for an increased number of wavelengths and increased the Zernike polynomials expansion to the ninth order. The system polychromatic mean square wavefront deformation $(\Delta\Phi)^2$ became

$$(\Delta\Phi)^2 = \frac{1}{5} \sum_{i=1}^5 \left\{ \frac{[C_{20}^{\text{new}}(\lambda_i)]^2}{3} + \frac{[C_{40}(\lambda_i)]^2}{5} + \frac{[C_{60}(\lambda_i)]^2}{7} + \frac{[C_{80}(\lambda_i)]^2}{9} + \frac{[C_{100}(\lambda_i)]^2}{11} \right\}. \quad (2)$$

We then used the improved 2GS global search 5λ algorithm with the updated glass catalog to look again for the optimal designs for $f = 12$ mm F/1.7 470–650 nm camera and a longer focal length lens needed for the AWARE 2 Gigapixel imager, with $f = 70$ mm, F/3.5, and a 486–656 nm spectrum.

For the $f = 12$ mm case, the previously optimal top family of solutions remained on top while quite a few intermediate (but still inferior) families were generated (Table 1). For simplicity, since there are many similar glasses in the catalogs, a number of glasses that have a refraction index within ± 0.03 and an Abbe number within ± 2 of the glasses shown we considered as replacement glasses and omitted from the table.

On the other hand, the longer $f = 70$ mm lens benefited significantly from the increased number of materials, and we identified two better candidate families than previously reported: K-VC82/P-LAF37/S-BAH11/K-LasFN10 with a CAF2 core [as shown in Fig. 4(a)] and M-LAF81/MP-LAF81/L-LAM69/S-LAH60 with K-GFK68 core [as shown in Fig. 4(b)].

The monocentric 2GS global search generates a full list of ranked solutions, which is why a global search algorithm is more powerful than simply doing guided hammer/global searches in a commercial optical design software like ZEMAX or CODEV. From a ranked list, the lens designer can quickly choose the specific designs subject to specific constraints such as lens volume, differential thermal expansion, or glass material availability.

B. Three-Glass Symmetric Global Search

After reaching the 2GS architecture limits, we explored the 3GS architecture shown in Fig. 5. Similar to 2GS geometry, from the first order principles, the focal length is given by [8,16]

$$\frac{1}{f} = \frac{2}{r_1} \left(1 - \frac{1}{n_2}\right) + \frac{2}{r_2} \left(\frac{1}{n_2} - \frac{1}{n_3}\right) + \frac{2}{r_3} \left(\frac{1}{n_3} - \frac{1}{n_4}\right) \quad (3)$$

Table 1. Updated List of Top Solutions for the SCENICC F/1.7 $f = 12$ mm 470–650 nm 120° Monocentric Lens*

No.	Outer Glass	Internal Glass	Fast Exact Ray Tracing [mm]			ZEMAX Optim. Radii [mm]		MTF at 200 lp/mm
			R1	R2	$(\Delta\Phi)^2$	R1	R2	
1	S-LAH79	K-LaSFn9 , TAF5, S-LAH59	9.060	3.781	0.00547	9.068	3.792	0.648
2	TAFD55 (LASF35)	K-LaFK50 , S-YGH52, M-TAC60...	8.529	3.800	0.00618	8.533	3.807	0.622
3	N-LASF46A/B (TAFD25, L-LAH86)	M(C)-TAF1 , TAF5, K-LaFK50(T), S-LAH59, K-LaSFn9, S-LAH65(V)...	9.057	3.614	0.00622	9.065	3.630	0.609
4	L-NBH54	K-LaFn9 , S-LAM55	8.949	3.629	0.00633	8.960	3.649	0.606
5	K-GIR79 (LAH80, N-LASF9)	K-LaFK50T , M(C)-TAF1, N-LAF21, K-LaSFn16, TAF4...	9.290	3.435	0.00637	9.300	3.456	0.591
6	TAFD40	M-TAFD305 , L-LAH85V, L-LAH83	9.533	3.730	0.00749	9.537	3.735	0.626
7	S-LAH79	M-TAF101 , N-LAF21, K-LaSFn16, TAF4, M-TAF1, TAC4, K-LaKn12...	8.470	3.802	0.00757	8.477	3.814	0.626
8	K-PSFn5	N-LASF45(HT) , S-LAM66	9.348	3.600	0.00793	9.357	3.617	0.607
9	TAFD40	N-LAF2 , K-LaF2, LAF2, S-LAM2, K-LaFn11, S-LAM61...	8.191	3.792	0.00795	8.194	3.796	0.592
10	LASF35 (S-LAH79)	K-LaK9 , K-LaK12, N-LAK12, S-LAL12...; K-VC80 , K-LaK13 , P-LAK35 , L-LAL13 , S-LAL13 ...	7.487	3.746	0.00856	7.492	3.752	0.561
11	N-LASF46A/B (TAFD25, L-LAH86)	N-LAK12 , K-LaK9, N-LAK12, S-LAL12, LAC12, L-LAL12...	7.813	3.701	0.00886	7.817	3.707	0.534

*Prescriptions shown pertain to glass combinations, marked in bold.

For each chosen glass combination, one radius is a function of the other two radii and the predefined focal length target value.

From the real ray-trace geometrical equations we obtained

heights. To allow for extended spectral bands and material dispersion curves, a ray trace is done for nine equally spaced wavelengths inside the spectrum of interest. In the 3GS geometry there is around 220 million glass combinations, and the optimization

$$\overline{OE} = \frac{h}{\sin \left\{ 2 \left[\arcsin \left(\frac{h}{r_1} \right) - \arcsin \left(\frac{h}{r_1 n_2} \right) + \arcsin \left(\frac{h}{r_2} \right) - \arcsin \left(\frac{h}{r_2 n_3} \right) + \arcsin \left(\frac{h}{r_3} \right) - \arcsin \left(\frac{h}{r_3 n_4} \right) \right] \right\}}. \quad (4)$$

The longitudinal aberration for the ray with input height h_i is given by

$$\Delta S(h_i) = \overline{OE}(h_i) - f \quad (5)$$

Finally, we constructed the following merit function for 3GS geometry optimization:

$$Q = \sum_{i=1}^9 \sum_{j=1}^8 p_j \cdot \text{Abs}(\Delta S(h_j, \lambda_i)) = \sum_{i=1}^9 \sum_{j=1}^8 p_j \cdot \text{Abs}(\Delta S(p_j \cdot f \cdot NA, \lambda_i)), \quad (6)$$

where f is the focal length of the lens, NA the numerical aperture, and $p = [1, 0.9, 0.8, 0.7, 0.6, 0.5, 0.4, 0.3]$ are the pupil zones used to calculate eight ray

problem is inherently two-dimensional. In an attempt to reduce the computing time to reasonable limits, we identified and made use of an interesting fact about 3GS geometries. In the two-dimensional optimization space of the 3GS monocentric system, if the glass choice is viable, areas of minimum merit

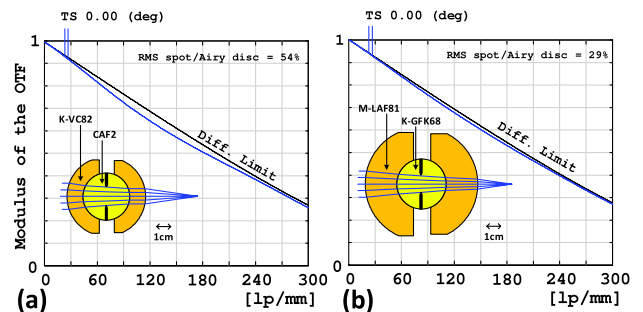


Fig. 4. New $f = 70$ mm AWARE 2 2GS candidates.

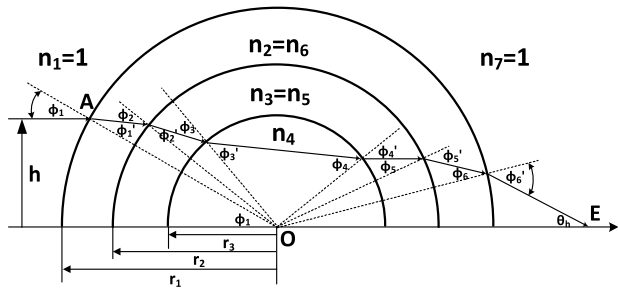


Fig. 5. Monocentric three-glass symmetric (3GS) architecture.

function (high performance) look like a long and nearly linear ravine [Fig. 6(a)].

So it is possible to fix the radius of the second glass shell at two points with some reasonable values, cross the ravine at two r_2 levels to get its orientation, and then trade the two-dimensional optimization problem for one-dimensional track along the ravine. This increased the computational efficiency and made it possible for the global search to run in 24–48 h on a high-performance workstation (4×2.7 Hz Intel Xeon E5-4650). Because the ravine is substantially flat at the bottom, we had the freedom to choose the second radius in 3GS system, and this was helpful in avoiding excessively thin shell solutions, which are impractical to fabricate. Figure 6(b) shows the comparison of 2GS and 3GS top candidates for the 12 mm F/1.7 monocentric lens operating in the extended visible (435–850 nm) waveband. Both solutions are strong apochromats [Fig. 6(c)], but unfortunately the 3GS geometry offered only modest performance improvement in MTF and the spot size. A similar result is observed when the global 3GS search is applied in all scenarios for the $f = 12$ mm imager lens variants discussed in Section 1 of this paper. 3GS global search generates a number of high-ranked solutions that have nearly identical performance, and it is difficult to say which one is the absolute best performer. Some solutions have slightly better MTF but worse RMS spot size, and vice versa. The candidates shown in Fig. 7 are chosen by MTF performance.

An interesting fact about the 3GS geometry is that all good solutions are always derivatives from the good 2GS candidates. In other words, glass core materials of the top candidates identified in 2GS global search also form top 3GS solutions. That kind of behavior was observed in all design scenarios. Therefore the “quick track” to global 3GS solutions may be the exploration of all glass combinations, constrained only by the limited number of materials for the core. This effectively reduces the CPU computing time from days to hours or, in the case of GPU computing, from hours to minutes. After a number of global 3GS searches and comparisons, we finally concluded that over the scale of apertures and waveband parameters we considered here, the 3GS architecture does not offer a significant performance improvement over the 2GS architecture.

C. Seeded Hammer Optimization

For the desired monocentric lens specification, as a start, a 2GS global search was performed and the full list of ranked candidates was created. Then, the multiple top candidate prescriptions were imported to ZEMAX and manual lens splitting and air gap introduction were performed: first guiding the candidate optimization to 3GA-7 structure, and then to 4GA-8 structure. All glass materials were substitution variables except the core, and within hours (sometimes even minutes) Hammer search would find a useful solution. We must emphasize that in order for that to happen, the most important thing is a good starting core material for the given design. Without 2GS global search algorithm input, both ZEMAX and CODEV may have a hard time converging to the best solutions if the starting design core material is not close to the ideal, especially for the low F-number cases.

The reason for that was the shape of multiple local minimums in the monocentric design space as discussed in the previous paper [8]. Optimized 4GA-8 structures through the ZEMAX Hammer optimization seeded from top 2GS candidates of the modified 12 mm imager specification lenses are shown in Fig. 8. The original lens [Fig. 8(a)] was substantially

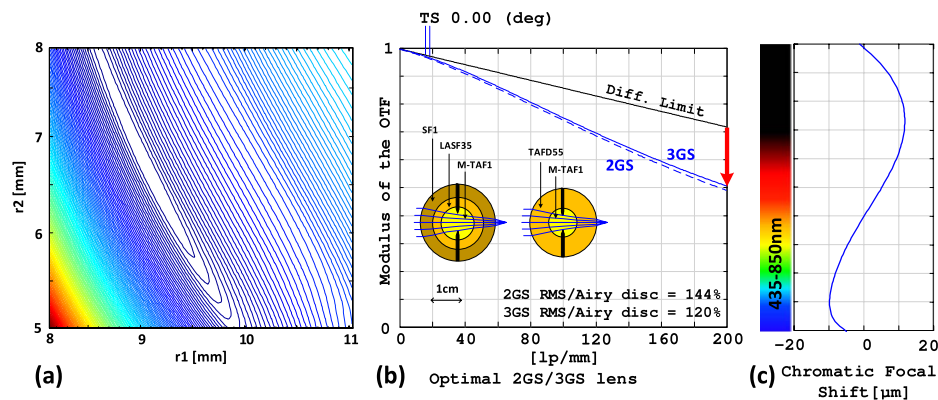


Fig. 6. Top 12 mm F/1.7 435–850 nm 3GS monocentric lens candidate (a) optimization space, (b) MTF comparison curves with top 2GS candidate, and (c) apochromatic shaped focal shift curve.

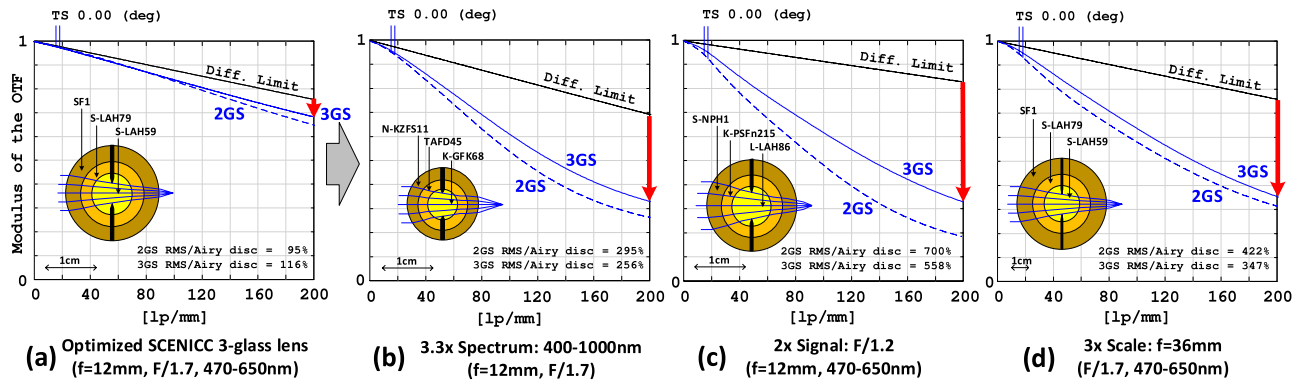


Fig. 7. MTF performance comparison of globally optimized 2GS and 3GS monocentric lenses for extension of the original lens specifications. The plots show only on-axis MTF, to allow comparison of 2GS and 3GS architectures.

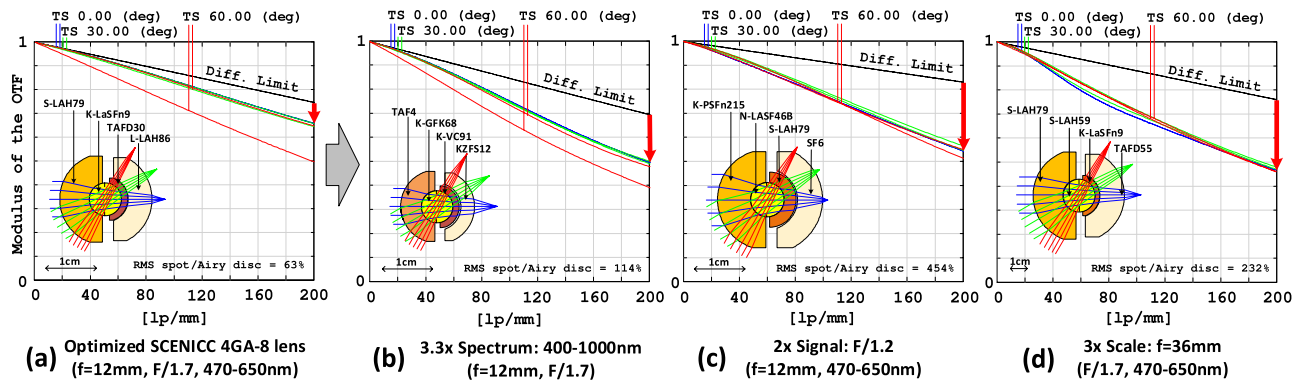


Fig. 8. MTF performance curves of the 4GA-8 lens geometries derived from the original lens specifications through seeded Hammer optimization.

diffraction-limited in both the 2GS and 3GS geometry, so with the original design specification only a slight improvement is seen.

For the other three cases, however, the more complex lens achieved substantial performance improvement. Hammer optimization is not global, and even higher performance designs may exist, so the 4GA-8 architecture is a promising choice for high-performance lenses. This lens is sufficiently complex that an exhaustive and truly global optimization is impractical, but in the following section we describe a five-dimensional 4GA-8 monocentric architecture optimizer to identify “near-global” lens designs.

D. Five-Dimensional 4GA-8 Near Global Optimization

A useful solution is to break the front/rear symmetry and introduce an asymmetric air gap between the crown and flint glass core [5,19]. Introducing such an air gap is a common method used for control of spherochromatism [20–22]. This approach yields the four-glass air gap asymmetric geometry, which improves performance on extended spectral bands, larger apertures, and longer focal length systems. The four-glass with air gap (4GA-8) lens architecture is shown in Fig. 9.

Attempts to optimize the four-glass architecture with ZEMAX software shows that the result of optimization strongly depends on the initial starting

point position. Some results obtained from very different starting points in the radii space showed good image quality but others were trapped in lower quality pockets. Such behavior of the commercial lens design software indicates that the optimization space

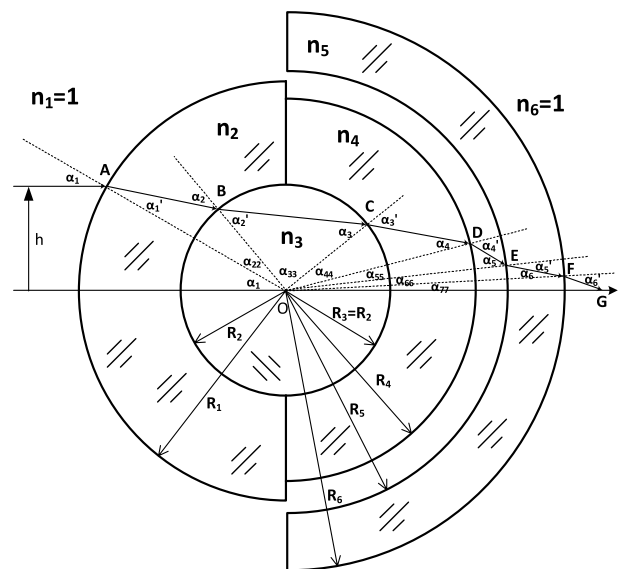


Fig. 9. Four-glass asymmetric with air gap (4GA-8) monocentric lens architecture.

of the 4GA-8 monocentric lenses has some specific features that must be investigated and special optimization algorithms to be developed. As for the 2GS and 3GS architectures, for lens quality evaluation we used fast exact monocentric lens ray tracing. For the input ray at height h it gives the value for the length OG (all radii values assumed positive):

$$\overline{OG} = \frac{h}{\sin \left\{ \arcsin\left(\frac{h}{R_1}\right) + \arcsin\left(\frac{h}{R_2 n_2}\right) + \arcsin\left(\frac{h}{R_2 n_4}\right) - \arcsin\left(\frac{h}{R_1 n_2}\right) - 2 \arcsin\left(\frac{h}{R_2 n_3}\right) \right.} \quad (7)$$

$$\left. + \arcsin\left(\frac{h}{R_4}\right) - \arcsin\left(\frac{h}{R_4 n_4}\right) - \arcsin\left(\frac{h}{R_5}\right) + \arcsin\left(\frac{h}{R_5 n_5}\right) + \arcsin\left(\frac{h}{R_6}\right) - \arcsin\left(\frac{h}{R_6 n_5}\right) \right\}$$

The longitudinal aberration $\Delta S(h_i)$ for this ray will be

$$\Delta S(h_i) = \overline{OG}(h_i) - f, \quad (8)$$

where f is the focal length. To form the optimization criterion, the results of fast exact ray tracing with Eqs. (7) to (8) were used. The entrance heights h of these rays are

$$h_i = \text{NA} \cdot f \cdot p_i, \quad (9)$$

where p_i is an array of reduced rays heights at the pupil. The array is defined as

$$p = \begin{bmatrix} 1 & 0.97 & 0.88 & 0.8 & 0.7 & 0.6 & 0.5 & 0.4 & 0.05 \end{bmatrix}. \quad (10)$$

For the optimization criterion C , the following sum was used:

$$C = \sum_{i=1}^9 \sum_{j=1}^9 \left[p_j \cdot \frac{\Delta S(h_i)}{\lambda_j} \right]^2 + [\Delta S(h_9, \lambda_1) - \Delta S(h_9, \lambda_9)]^2$$

$$+ [\Delta S(h_3, \lambda_1) - \Delta S(h_3, \lambda_9)]^2$$

$$+ [\Delta S(h_1, \lambda_1) - \Delta S(h_1, \lambda_9)]^2, \quad (11)$$

where λ_j is the wavelength in micrometers used for weighting. The first term of the criterion C equation is a sum of squared values proportional to lateral aberrations and the following three members are squared chromatic longitudinal aberrations differences at the pupil reduced rays heights 1, 0.88, and 0.05. The longitudinal chromatic difference at the reduced pupil height 0.05 is similar to the classical chromatic focus shift. Pupil points with reduced pupil height 1 and 0.88 are critical for the spherochromatism correction. For optimization of any monocentric lens operating in an extended waveband, we used nine wavelengths. For example, for criterion calculations for monocentric lenses designed to operate with a front-illuminated silicon

CMOS or CCD sensor, we used the waveband 0.4 to 1.0 micrometers, divided into eight equal segments at nine wavelength values.

This criterion demonstrated a good correlation with modulation transfer function (MTF) for all types of monocentric lenses operating in extended wavebands.

The starting point for the 4GA-8 systematic search is to make use of the core from multiple 2GS top candidates as seeds for further optimization. The most promising glass K-GFK68 was chosen as a basic core glass for the systematic solution search, and then the other glasses were replaced in all possible combinations. For each glass combination, the search of minimum of the criterion C [Eq. (11)] was performed and the optimized system was found. With the chosen glass combination we have five radii to optimize. In fact there are seven radii in the optical scheme, including the image surface radius (Fig. 9), but the third radius is equal and opposite to the second radius because the use of the central ball lens, and the image surface radius must match the focal length.

Investigation of the criterion C behavior showed the multi-extremum nature of the function being optimized. But in our case, on top of this problem, we have a number of linear combinations between optimization parameters, or in other words, lines and surfaces in the optimization space over which the criterion does not change or changes very slowly. The optimization process is stuck somewhere in these ravines depending on the starting point position. Such areas are multidimensional ravines or saddle type stationary areas.

For each glass combination, the minimum value of the criterion C is located at different positions in the radii space, but all glass combinations still have the characteristic general shape of solutions in the 5D radii space. For every glass combination, the contour surfaces with the constant values of criterion C around the minimums appear as thin, "pancake-shaped" volumes in the 5D radii space. These thin pancake volumes are pierced with a net of saddle type ravines, and are connected over the main ravine. Applying conventional optimization methods results in slow convergence to a solution trapped in the saddle type ravines, rather than the global minimum [23,24]. The behavior of the gradient method in such cases is illustrated in Fig. 10 (adapted from [24]). Figure 10(a) shows the gradient method behavior in the general case of the normal minimum shape. The gradient descent direction at any step is directed orthogonally to the criterion contour line

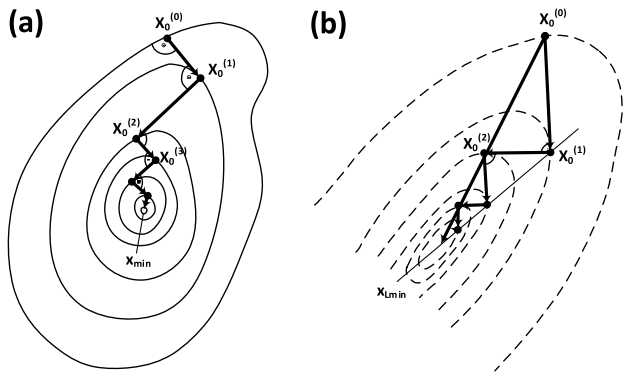


Fig. 10. Gradient descent method applied for normal minimum and degraded minimum shape.

and straight descent is continued up to the point when it reaches another lower value contour line for which the direction of descent would be tangential.

The process converges quickly to the minimum in just a few steps. In the case of a degraded (stretched) minimum with the strong linear dependence between optimization parameters, as shown in Fig. 10(b), the gradient method begins to oscillate. In [25], the method of conjugated gradients was proposed. It was shown that apexes of segmented lines in the gradient method are located on the lines showing the direction to the minimum and after several steps we can create these lines by using the least square method. The move along these lines will facilitate a fast descent to the minimum.

While the method of conjugated gradients can help in a number of degraded minimum cases, our situation is more sophisticated. The minimum volume has the shape of a thin pancake in the 5D space, with the walls close to being parallel, such that gradient descent segments $X_0^i X_0^{i+1}$ and $X_0^{i+1} X_0^{i+2}$ will practically coincide. The points X_0^i , X_0^{i+2} , X_0^{i+4} will be located so close to each other that we will not be able to reliably connect them with the line. Moreover, all the points inside the five-dimensional thin pancake minimum area are saddle-like points. At every point we have Hesse matrix [23,26] having one nearly zero negative eigenvalue, demonstrating a strong linear dependence between the first (R1) and last (R6) radii, while other eigenvalues will be strongly positive. The saddle type nature of the area of the minimum solution is another reason that conventional optimization methods are likely to be trapped at different points inside the pancake, where the specific endpoint depends sensitively on the initial starting point of the optimization. In this situation, even the method of conjugated gradients fails.

The optimization of our lens architecture required the development of special methods, which we will illustrate using the example of a lens with the following glass combination: P-LASF47, K-GFK68, K-LASFN6, and N-KZFS11. This glass combination demonstrated sufficiently good performance during our search for the optimal solution and was chosen

as an example to demonstrate the optimization procedure.

Our search for the near minimum begins with a gradient descent [23] to the closest local minimum from the average radii solution for this architecture (Fig. 9). The optimization of this glass combination begins from the average radii combination at point $M0 = (7.0, 2.9, -2.9, -4.2, -4.5, -7.8, -12.0)$, in millimeters. The value of the criterion C [Eq. (11)] at this point is 13.23. The local gradient descent method quickly arrives to the point inside pancake area with radii array $M1 = (7.06457, 2.95860, -2.95860, -4.16102, -4.46400, -7.74390)$, which again are shown in millimeters, and criterion value at this point is $C = 0.00709$. The contour lines graphs of the criterion C [Eq. (11)] in the plane section of radii R1-R6 of the five-dimensional space is shown in Fig. 11.

The minimum area is a thin long strip, which is the section of a five-dimensional thin pancake. The minimum point M1 is shown with information box on Fig. 11(a). We used the Hesse matrix eigenvectors [26] to find the direction of the strip. The five eigenvalues of the Hesse matrix at this point are $-0.01024, 0.25782, 0.91727, 25.44,$ and 21148.91 . Note that radius number three does not participate in the optimization because it is equal to the negative value of the second radius. The two eigenvectors having smallest eigenvalues are $E1 = (-0.60071, 0.00309, -0.00223, 0.00967, -0.79988)$ and $E2 = (0.31650, 0.12960, -0.50686, -0.75252, -0.24462)$, where the eigenvector direction cosines are related to the radii R1, R2, R4, R5, and R6, respectively. The section of criterion C shows that the main ravine is related to the eigenvector E1. We will name this ravine as the main virtual ravine (Fig. 12).

Knowing that gradient methods are descending in the direction orthogonal to the contours of constant criterion C value, it is not surprising that gradient methods from any initial point come toward the main virtual ravine but to different locations over this ravine depending on the location of the initial point. The 3D graph of the criterion C with dependence on the first and last radii is shown in Fig. 11(b). The value of the criterion function C in the direction orthogonal to the ravine quickly reaches the value of 0.25, with

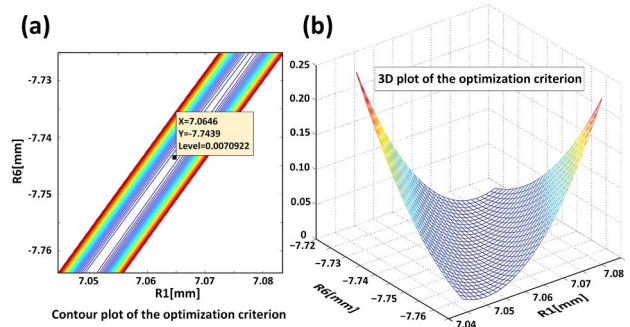


Fig. 11. Optimization criterion ravine of minimums (projection onto 3D space).

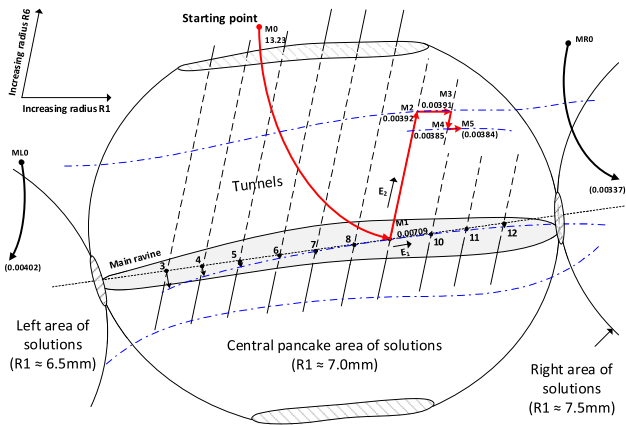


Fig. 12. Optimization procedure inside the 4GA-8 optimization space.

radii space step size as small as 0.02 mm. We will use the main ravine as an entrance area into the pancake space. The ravine is located very close to the straight line associated with the eigenvector E1 (the black dotted line in Fig. 12). We travel over this straight line that is defined by the first eigenvector direction at the point of the minimum M1 and make a number of local optimizations, which will quickly come to the actual lowest point of the ravines.

Following over the direction of eigenvector E1 we made 17 steps with 0.05 increments in the radii space (8 steps in the direction of lower first radius and 8 steps in the opposite direction) and, making the gradient descent from each point, obtained the array of minimums. Table 2 shows the central 10 minimums (ravine bottom points) of this scan with minimum M1 over the main ravine at place number 9. Table 2 shows that minimums are located over a deep and slightly curved ravine, with a strong linear dependence between the first and last radii.

The body of the pancake shaped minimum is located over the 3D sphere inside the 5D space, and this sphere is orthogonal to the ravine, as shown in Fig. 11(b). The directions of the minimum increment of the criterion C at each bottom point over the ravine is a direction of the second eigenvector while the first one is still directed over the ravine. The tunnels into the pancake (black dashed lines in Fig. 12) [26] are located over the directions of second eigenvectors. These vectors are orthogonal to the ravines (blue dash-dot lines in Fig. 12).

To find the point of the criterion C minimum we crossed the ravine structure inside the pancake area of solutions from the point M1 in the direction of the second eigenvector E2. Then we initiated local gradient descents with the step of 0.025 mm. Values of C over this line after local gradient descents are 0.00709 (point M1), then [0.00622, 0.00558, 0.00504, 0.00470, 0.00439, 0.00412, 0.000400, 0.00393, 0.00392, 0.00399]. The ravine with the minimum value of criterion C is at the point M2, having $C = 0.00392$ and the array of radii is $M2 = (7.13558, 2.98846, -2.98846, -4.27410, -4.63395, -7.79880)$. Then we made 17 steps along eigenvector E1 of this ravine with the short gradient descent. The values of C over ravine are [0.00431, 0.00424, 0.00413, 0.00405, 0.00401, 0.00399, 0.00394, 0.00395, 0.00393, 0.00392, 0.00391, 0.00394, 0.00395, 0.00396, 0.00404, 0.00413, 0.00418]. The minimum value of $C = 0.00391$ is at the point M3 with array of radii $M3 = (7.10544, 2.98890, -2.98890, -4.27469, -4.63355, -7.83869)$.

We performed this whole operation in cycles until the step when the minimum is located at the initial point of the last cycle. The whole optimization path is shown by the solid red line in Fig. 12.

Values of C around M3 are [0.00426, 0.00425, 0.00405, 0.00391, 0.00385, 0.00388, 0.00394], where the new minimum point M4 has $C = 0.00385$, and array of radii $M4 = (7.09785, 2.98510, -2.98510, -4.26180, -4.61467, -7.83319)$. The next step along this new ravine associated with the point M4 gives the point M5 at one step from M4 with $C = 0.00384$. The array of radii at M5 is $M5 = (7.08293, 2.98531, -2.98531, -4.26206, -4.61453, -7.85324)$.

The next crossing of the ravines did not succeed and the minimum C point remained at the point M5, indicating that we had approached the limit of this process. The next step was to substitute the array of radii at the point M5 with $C = 0.00384$ into ZEMAX software, where we obtained the MTF value of 0.54 at 200 lp/mm frequency. After that we used the standard Zemax process for a local optimization of the optical prescription to obtain the maximum MTF. The final results are shown in Table 3. For the MTF optimized scheme MTF at 200 lp/mm is 0.567. It is slightly better than we had at the optimum point of criterion C (Eq. 11). The construction

Table 2. Array of Local Minimums Over the Main Ravine in 4GA-8 Optimization Space.^a

	5	6	7	8	9	10	11	12	13	14
C_{initial}	0.0132	0.0089	0.0074	0.0071	0.0071	0.0071	0.0075	0.0092	0.0135	0.0220
r_1	6.945	6.975	7.005	7.035	7.065	7.010	7.125	7.155	7.186	7.216
r_2	2.959	2.959	2.959	2.959	2.959	2.959	2.958	2.959	2.956	2.957
r_3	-2.959	-2.959	-2.959	-2.959	-2.959	-2.959	-2.959	-2.963	-2.956	-2.957
r_4	-4.162	-4.162	-4.161	-4.161	-4.161	-4.161	-4.161	-4.161	-4.161	-4.161
r_5	-4.462	-4.462	-4.463	-4.463	-4.464	-4.464	-4.465	-4.465	-4.466	-4.466
r_6	-7.904	-7.864	-7.824	-7.784	-7.744	-7.704	-7.664	-7.624	-7.584	-7.544
C_{final}	0.0072	0.0071	0.0071	0.0071	0.0071	0.0071	0.0072	0.0073	0.0075	0.0078

^aRadii shown pertain to the areas at the bottom of the ravine reached after optimization.

Table 3. Optical Prescription of the 400–1000 nm $F/1.7 f = 12$ mm MC Lens Example Solution A = 5.63 g

	Radius	Thickness	Glass	Semi-Diameter
OBJ	Infinity	Infinity		Infinity
1	7.05918	4.10337	P-LASF47	6.75121
2	2.95581	2.95581	K-GFK68	2.93356
STO	Infinity	2.95581	K-GFK68	2.20989
4	-2.95581	1.26426	K-LASFN6	2.91646
5	-4.22007	0.35576		4.05564
6	-4.57583	3.27037	N-KZFS11	4.34140
7	-7.84620	4.14501		7.12060
IMA	-11.9913			10.38526

of a low burden computer criterion from the results of raytracing, which will perfectly correlate with MTF performance, is still an open problem [24,27]. However, we consider that our criterion is in good correlation with MTF, allowing us to sort the results of the search for 4GA-8 architecture.

The optimization process from the different initial point MR0 having $R1 = 7.5$ mm shows another solution inside the neighboring pancake area on the right (Fig. 12), with the value of $C = 0.00337$. The optimized MTF at frequency 200 lp/m for this solution is 0.575. The optical prescription is shown in the Table 4.

Similarly, the next optimization process from the initial point ML0 having $R1 = 6.5$ mm shows another solution inside the neighboring pancake on the left with $C = 0.00402$. The optimized MTF at frequency 200 lp/m for this solution is 0.562. The optical prescription is shown in the Table 5. In the global

Table 4. Optical Prescription of the 400–1000 nm $F/1.7 f = 12$ mm MC Lens Example Solution B = 5.71 g

	Radius	Thickness	Glass	Semi-Diameter
OBJ	Infinity	Infinity		Infinity
1	7.26696	4.34654	P-LASF47	6.93839
2	2.92041	2.92041	K-GFK68	2.89944
STO	Infinity	2.92041	K-GFK68	2.20692
4	-2.92041	1.29818	K-LASFN6	2.88460
5	-4.21859	0.41330		4.05796
6	-4.63189	3.00543	N-KZFS11	4.39123
7	-7.63733	4.35056		6.95098
IMA	-11.98789			10.38221

Table 5. Optical Prescription of the 400–1000 nm $F/1.7 f = 12$ mm MC Lens Example Solution C = 5.72 g

	Radius	Thickness	Glass	Semi-Diameter
OBJ	Infinity	Infinity		Infinity
1	6.56181	3.55968	P-LASF47	6.30232
2	3.00213	3.00213	K-GFK68	2.97882
STO	Infinity	3.00213	K-GFK68	2.21707
4	-3.00213	1.16917	K-LASFN6	2.95718
5	-4.17130	0.24397		4.00443
6	-4.41527	4.06139	N-KZFS11	4.19853
7	-8.47720	3.51334		7.62830
IMA	-11.99054			10.38469

search among these three feasible solutions we prefer the solutions of first type shown in Table 3, as they have the smallest weight.

The procedure described above was applied on all other glass combinations, and our near-global search resulted in 350 top solutions that are grouped in seven distinctive families (Table 6). Glasses are considered replacement glasses if their index of refraction is within ± 0.03 range and Abbe number in ± 3 range of glasses shown in the table.

The example solution discussed before, shown in Tables 3–5, belongs to the first family of solutions. Figure 13 shows the optical layout of the lens and MTF curves of the top solution from the first family and compares it with the seeded Hammer result from Fig. 8(b). The prescription of this near-global optimum solution is shown in Table 7. Upon inspection of the full solutions list, the seeded Hammer solution was located with $C = 0.006354$ near-global search criterion value and obviously far outside the top solutions families.

Our near global 5D search improved the MTF performance at 200 lp/mm over the seeded Hammer solution by a 16% margin. Figure 14 shows graphs of sensitivities of the front and back-illuminated silicon sensors [28].

Our next goal was to modify the 400–1000 nm 4GA-8 solution from Table 3 to operate with front-illuminated silicon sensor.

We constructed ZEMAX merit function as a function keeping at minimum radii of point spread functions at all nine wavelengths (operators REAR), maximizing MTF at frequencies 100, 160, and 200 lp/mm and keeping the focal length at 12 mm (operator EFFL).

Substitution of the wavelength weights for the front-illuminated silicon sensor and quick reoptimization in ZEMAX gave the optical prescription shown in Table 8.

The image quality is practically diffraction limited. The MTF of the lens is shown in the Fig. 15. At the 200 lp/mm the lens has 90% level of diffraction limited resolution. Back-illuminated silicon sensors are sensitive to as low as 200 nm wavelength. We found that achromatization in 200–1050 nm waveband is out of ability of the 4GA-8 architecture at this scale and aperture.

In order to avoid the use of expensive coatings we decided to cut off the UV spectrum by using the mounting meniscus made from the Schott GG435 absorptive glass. Using an additional mounting meniscus at the curved image surface is optional and has little impact on imaging system performance.

The optical prescription of the monocentric lens operating with the back-illuminated silicon sensor is shown in Table 9. GG435 color glass refraction indices were measured with Filmetrix F10-RT refractometer. The MTF and the layout of the lens are shown in the Fig. 16. The image quality is close to diffraction limited.

Table 6. Families of Solutions for F/1.7 12 mm Monocentric 4GA-8 400–1000 nm Lens Obtained Through Near-Global Search

Family	1st Glass	2nd Glass (Core)	3rd Glass	4th Glass (Meniscus)	Near-Global Search Criterion	MTF at 200 lp/mm
I	P-LASF50	K-GFK68	TAF1	E-ADF10	0.003253	0.583
II	NBFD11	K-GFK68	TAF3	KZFS12	0.003572	0.569
III	L-LAM72	K-GFK68	TAF1	S-NBH53	0.003591	0.567
IV	TAF2	K-GFK68	P-LASF50	N-KZFS11	0.003808	0.577
V	L-LAH83	K-GFK68	NBF1	KZFS12	0.003958	0.555
VI	TAFD30	K-GFK68	P-LASF50	N-KZFS11	0.003970	0.559
VII	P-LASF51	K-GFK68	S-LAH58	N-KZFS11	0.003978	0.553

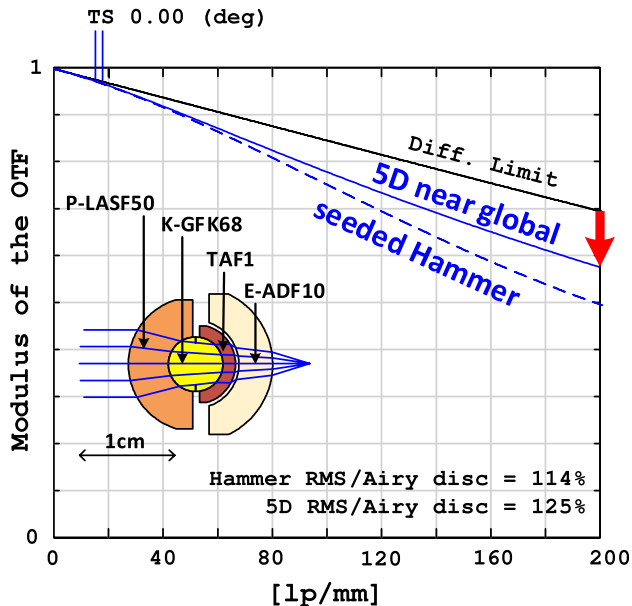


Fig. 13. MTF curves for 12 mm, F/1.7, 400–1000 nm lenses obtained through seeded Hammer search and near global five-dimensional optimization (shown on layout).

Both lenses have the core glass K-GFK68 with a very high coefficient of thermal expansion, TCE = 12.9, while surrounding glasses have low TCE coefficients. For example, the front-illuminated silicon sensor shown in Table 8: P-LASF47 glass has TCE = 6.04 and K-LASFN6 glass has TCE = 5.9. Normally the TCE difference less than 1.5 for cemented surfaces can be recommended for outdoor optics [29]. Recently Norland Products Inc. offered extremely low psi modulus NOA 76 [30]

Table 7. Optical Prescription of the 400–1000 nm F/1.7 $f = 12$ mm Monocentric Near Global Solution

	Radius	Thickness	Glass	Semi-Diameter
OBJ	Infinity	Infinity		Infinity
1	7.05656	4.20075	P-LASF50	6.75008
2	2.85581	2.85581	K-GFK68	2.83814
STO	Infinity	2.85581	K-GFK68	2.20709
4	-2.85581	1.30890	TAF1	2.82507
5	-4.16471	0.42696		4.00744
6	-4.59167	3.54357	E-ADF10	4.35045
7	-8.13525	3.84990		7.34868
IMA	-11.98514			10.37980

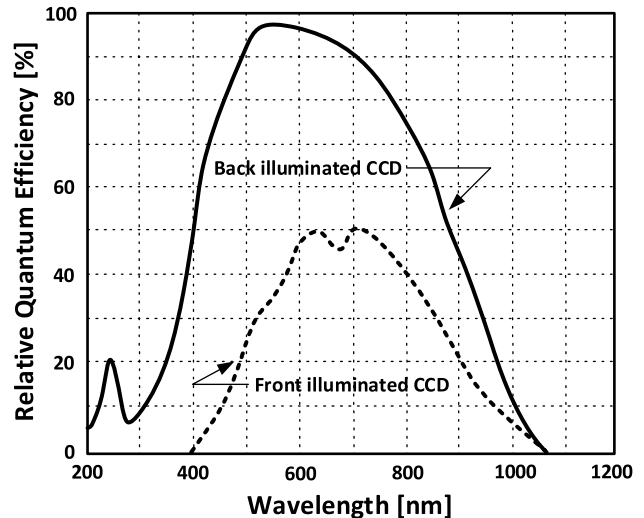


Fig. 14. Spectral response of front and back-illuminated silicon sensor.

optical cement, which can be used for glass pairs with such high CTE differences.

ZEMAX thermal modeling of the schemes shown in Tables 8 and 9 with a 10 micrometer thick layer of NOA 76 optical cement for differential thermal expansion shows that the lenses can operate in a wide temperature range of -20 C to +50 C without image quality degradation. Only a 0.02 mm back focal length adjustment is required. Since monocentric lenses were originally designed to be used with refocusing [8], this procedure does not pose a problem.

Finally, if we ask ourselves why the 4GA-8 architecture has such capabilities for achieving the high performance monocentric designs, the answer lays

Table 8. Optical Prescription of the 400–1000 nm F/1.7 $f = 12$ mm Monocentric Lens Operating with Front-Illuminated Silicon Sensor

	Radius	Thickness	Glass	Semi-Diameter
OBJ	Infinity	Infinity		Infinity
1	7.04107	4.08409	P-LASF47	6.73508
2	2.95699	2.95699	K-GFK68	2.93476
STO	Infinity	2.95699	K-GFK68	2.21103
4	-2.95699	1.26003	K-LASFN6	2.91758
5	-4.21702	0.35134		4.05282
6	-4.56835	3.30232	N-KZFS11	4.33494
7	-7.87067	4.12587		7.14073
IMA	-11.99654			10.38982

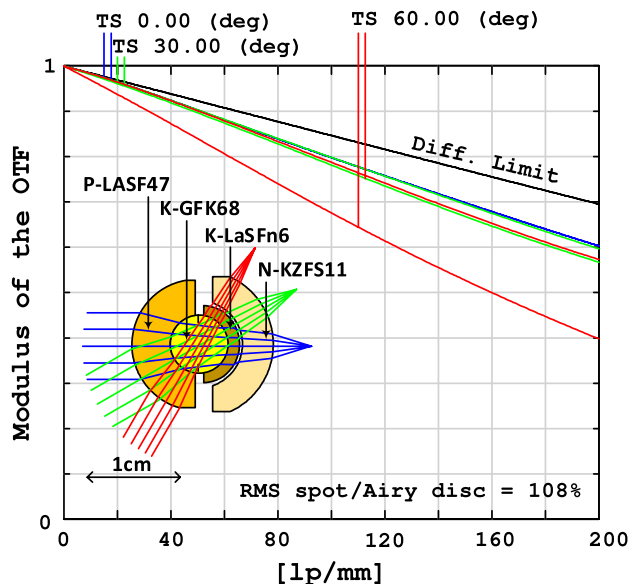


Fig. 15. MTF curves for 12 mm, F/1.7 lens operating with 400–1000 nm front-illuminated silicon sensor sensitivity spectrum.

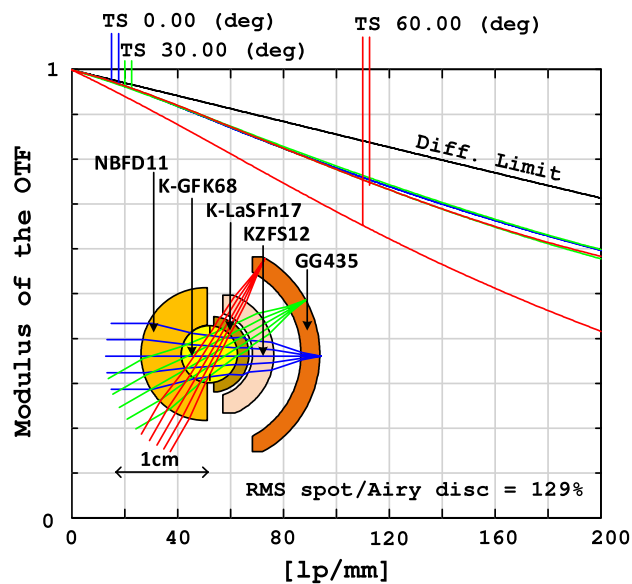


Fig. 16. MTF curves for 12 mm, F/1.7 lens operating with 435–1000 nm back-illuminated silicon sensor sensitivity spectrum.

Table 9. Optical Prescription of the 435–1000 nm F/1.7 $f = 12$ mm Monocentric Lens Operating with Back-Illuminated Silicon Sensor

	Radius	Thickness	Glass	Semi-Diameter
OBJ	Infinity	Infinity		Infinity
1	6.92285	4.01591	NBFD11	6.62605
2	2.90694	2.90694	K-GFK68	2.88753
STO	Infinity	2.90694	K-GFK68	2.21436
4	-2.90694	1.27374	K-LASFN17	2.87138
5	-4.18068	0.38453		4.02581
6	-4.56521	2.27558	KZFS12	4.33527
7	-6.84078	3.13995		6.28471
8	-9.98074	2.00000	GG435	8.75173
IMA	-11.98074			10.37606

in the asymmetry and the presence of an air-gap. To support that claim, on Fig. 17 longitudinal aberrations over the pupil for 3GS and 4GA-8 architectures are shown. Symmetric designs like 2GS and 3GS always have the shape of the longitudinal aberrations, as in Fig. 17(a).

This single bending curve, as the aperture grows, cannot be controlled, so the spherochromatism and zonal spherical aberration become dominant and limit the performance. On the other hand, presence of an air gap and broken symmetry help correcting those aberrations and adds an additional bending to the curve as in Fig. 17(b).

4. Lens Complexity and Performance Trade-off

To explore the maximum achievable performance of the monocentric lens geometries, we began with the design constraint of a 12 mm focal length 120° FOV imager and the visible waveband of 486–656 nm and optimized the lens design to increase the aperture as much as possible, subject to a predefined performance metric. This performance constraint was to require that the MTF was at least 70% of the

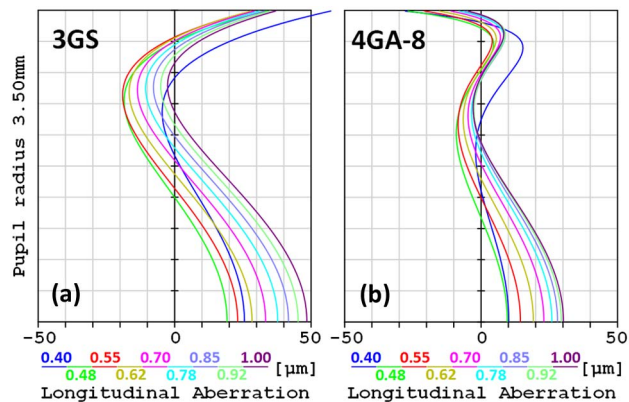


Fig. 17. Longitudinal aberrations of the (a) top 3GS and (b) top 4GA-8 architecture 12 mm F/1.7 monocentric lenses for 400–1000 nm spectral band.

diffraction limit at 200 lp/mm (the highest spatial frequency needed for Nyquist sampling of a 2.5 micrometer pitch Schott 24AS optical fiber faceplate) while simultaneously requiring that the RMS spot size radius had to be less than 1.5× the Airy disc radius (which maintained MTF at lower spatial frequencies). While this metric is somewhat arbitrary, the trends of the results are indicative of a wide range of related performance metrics, as applied to the available degrees of freedom. The results are shown in Fig. 18.

All chosen geometries, labeled in blue in Fig. 18 (1G-2, 2GAS, 3GA-6), converge to simpler ones and do not enable an increase in aperture size. The geometries labeled in black (1GS, 2GS, 3GS) show results obtained by our global optimization algorithm, while geometries labeled in red (3GA-7, 4GA8) are the result of the seeded Hammer optimization, starting from top 2GS candidates as seed designs.

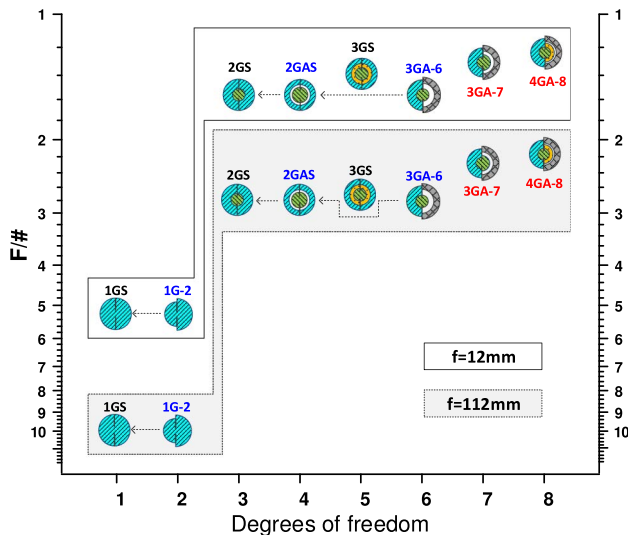


Fig. 18. Monocentric lens geometries optimization behavior for two different scales operating in 486–656 nm spectral range.

Adding the second glass is helpful in controlling the chromatic aberration, so there is a large increase in achievable F-number in moving from geometry 1GS to 2GS. This is equivalent to going from a singlet lens to a cemented doublet achromat. Adding the third glass in the 3GS geometry gives marginal

chromatic aberrations improvement over 2GS, whereas the other degrees of freedom (specifically, 2GAS with 4 DOF, and 3GA-6 with 6 DOF) provide no improvement.

Breaking the symmetry and introducing an air gap with the 7 DOF and 8 DOF architectures allows us to further increase the aperture, and still meet the desired MTF performance. Similar behavior is observed for the longer 112 mm focal length lens, which is also shown in Fig. 18.

The final step was to explore the design space for four different focal length scales ($f = 12$ mm (the SCENICC program lens scale), 40 mm, 70 mm (AWARE2 program [1]) and 112 mm (AWARE10 program [31])), and at each scale look at the maximum aperture for visible, extended visible, and visible-NIR spectral wavebands, subject to the MTF performance constraint described above. As before, we used the global optimization for the two-glass and three-glass symmetric systems (2GS, 3GS). For the three- and four-glass air gap candidates (3GA-7, 4GA-8), the combination of our systematic fifth-dimensional optimizer with ZEMAX hammer optimization was used. The entire set of results is summarized in Fig. 19. The clear trend is maintained over all three spectral bands and it shows the necessity of lens structure complexity

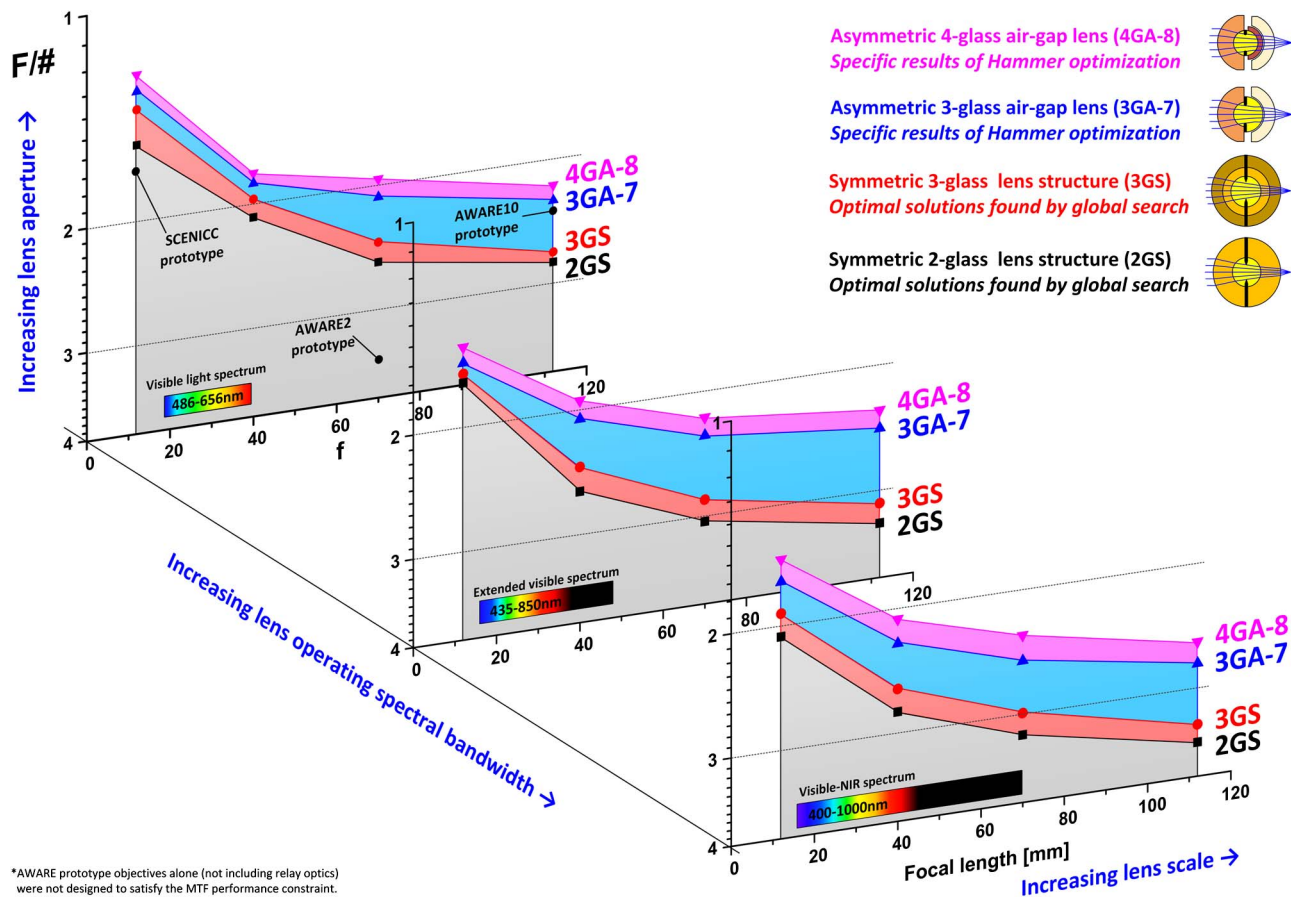


Fig. 19. Monocentric objective lens performance trade-off for different scales and three spectral bands (486–656 nm, 435–850 nm, 400–1000 nm).

increase if we wish to push the scale and/or the aperture size. For the time being, the area above pink 4GA-8 line remains *terra incognita* where the complexity and manufacturing cost increase outweighs the performance improvements. One exception to that rule is 5GA-10 architecture, which can be quite useful for medium scale (>100 mm) and large scale designs and will be demonstrated in an example in Section 5. 2GS global search still remains a powerful tool in monocentric lens design, both for supplying the final or seed designs for the more complex architectures. While the five-dimensional near-global search gives substantially better results over the 2GS seeded Hammer search, completing it on 32 CPU cores at this point is very time consuming and should be used only as a final attempt to squeeze out the maximum performance capability from the lens before manufacturing. Implementing the code for the 5D near global search on GPUs would possibly reduce the search time by a factor of hundred cutting it down from weeks to hours.

5. Specific Lens Design Examples

A. Water-Immersed Lens ($f = 12$ mm, $F/1.79$, 380–550 nm)

Water in natural reservoirs is highly scattering and lossy due to suspended particles, necessitating large NA optics for imaging at appreciable subsurface distances. The seawater transmission window is 300–600 nm, compatible with back-illuminated silicon sensors (Fig. 14). Underwater optics may also need to resist high pressure on the front lens. The large aperture of classical wide field underwater optics [10,32] must be protected by a window or dome, resulting in large weight and bulk.

Underwater objectives like the Gidrorussar model 11 ($f = 23$ mm) and 12 ($f = 11.9$ mm), which can achieve $F/2$ with a 40° – 60° overall field, have a thick cemented doublet as a front lens [32] and combine the Topogon structure with a Petzval projection lens for distortion compensation and image flattening over the 430–656 nm spectrum.

A 9 mm focal length $F/1.79$ monocentric underwater lens was optimized for the 0.38 to 0.55 micrometer spectral band. Table 10 shows the optical

Table 10. Optical Prescription of the Water Immersed Monocentric Lens

	Radius	Thickness	Glass	Semi-Diameter
OBJ	Infinity	Infinity	SEAWATER	Infinity
1	8.30000	2.00000	SEAWATER	7.61630
2	6.03999	3.48360	TAFD30	5.71884
3	2.55639	2.55639	N-LAF21	2.53267
STO	Infinity	2.55639	N-LAF21	1.87234
5	-2.55639	1.45793	LASF35	2.52255
6	-4.01433	0.15699		3.84362
7	-4.17132	2.61177	K-GIR79	3.96995
8	-6.78309	5.26472		6.24176
IMA	-12.04781			10.43447

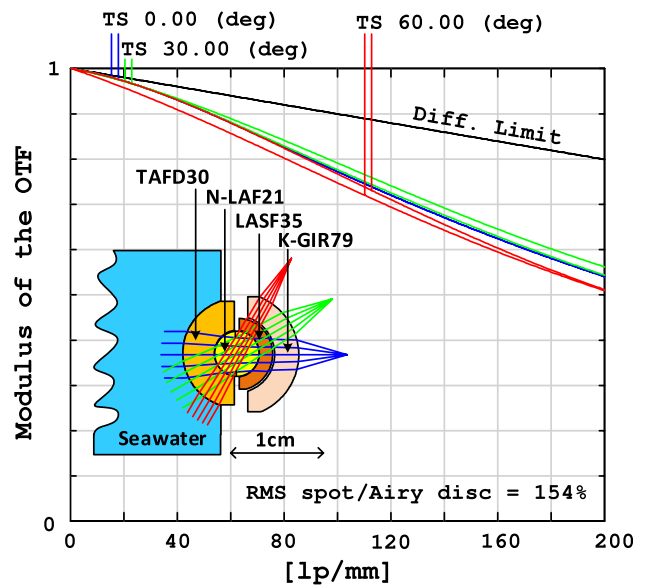


Fig. 20. Underwater monocentric lens (9 mm/12 mm image/object space focal length, $F/1.79$, 380–550 nm).

prescription of the 4GA-8 lens. The front lens is a cemented solid ball, which can support high pressure. The MTF of the underwater monocentric lens, shown in the Fig. 20, achieves 70% of the diffraction limit over a 120° full field of view.

B. Night Vision Lens ($f = 16$ mm, $F/1.2$, 500–900 nm)

Typical night vision goggles use image intensifiers operating from 700 to 900 nm and a lightweight (~ 40 g) 25 mm focal length $F/1.2$ objective lens covering a 40° field of view [33].

We found it possible to design a 120° wide field of view monocentric lens to satisfy these optical specifications, but the weight was 170 g. Scaling the lens to a 16 mm focal length matched the 40 g target weight. The resulting optical prescription is shown in Table 11. The $F/1.2$ lens operates from 500–900 nm, which spans the entire spectral band of the Gen III GaAsP photocathode. The lens resolves 100 lp/mm (Fig. 21), well over the 70 lp/mm supported by image intensifiers. While the resulting imager would provide some 50% lower angular resolution, it could operate over a 120° wide field, triple that of standard night vision optics.

Table 11. Optical Prescription of the Night Vision Monocentric Lens

	Radius	Thickness	Glass	Semi-Diameter
OBJ	Infinity	Infinity		Infinity
1	12.21344	7.19969	K-PSFN173	11.72988
2	5.01376	5.01376	K-GIR79	4.97624
STO	Infinity	5.01376	K-GIR79	3.67166
4	-5.01376	2.76625	K-PSFN173	4.92548
5	-7.78001	0.26457		7.36222
6	-8.04458	5.49005	KZFS12	7.55792
7	-13.53463	2.43761		12.03582
IMA	-15.97224			13.83509

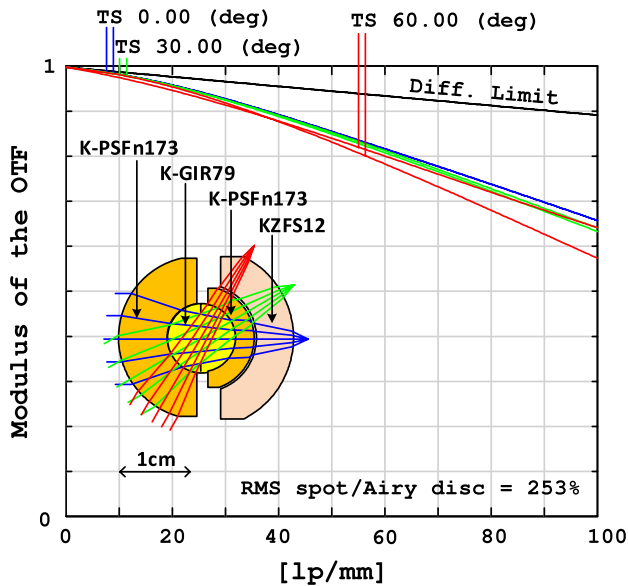


Fig. 21. Gen III Night Vision monocentric lens (16 mm focal length, F/1.2, 500–900 nm).

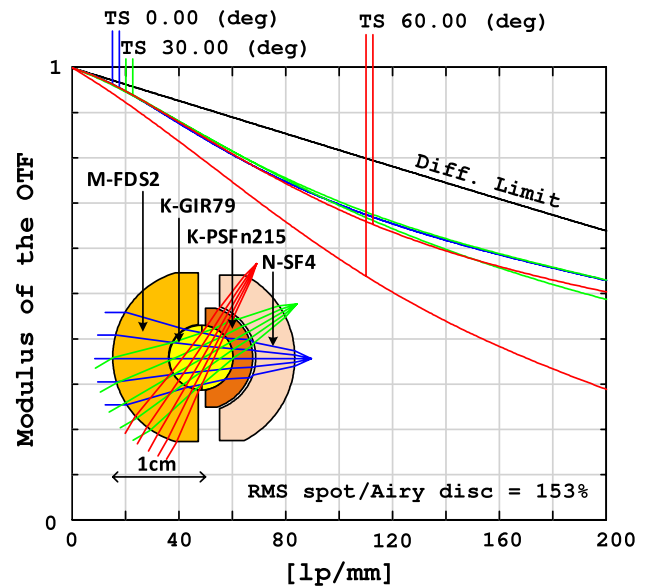


Fig. 22. SWIR monocentric lens (12 mm focal length, F/1.19, 900–1500 nm).

C. Short-Wave IR Lens ($f = 12$ mm, F/1.19, 900–1500 nm)

Skylight glow in the SWIR band provides a reliable light source for night imaging even in the absence of starlight [34].

This light can be sensed using uncooled InGaAs focal planes such as those available from Sensors Unlimited Corp. [35]. A 2GS seeded Hammer search produced the 12 mm focal length F/1.19 lens prescription shown in Table 12, with MTF and lens layout as shown in the Fig. 22. The lens provides nearly diffraction-limited resolution at 200 lp/mm, compared to the 33 lp/mm Nyquist frequency of the 15 μ m pixels in the 1280 \times 1024 Sensors Unlimited focal plane, and so monocentric optics will support advanced imaging even for the next generation SWIR sensors. The 15 g weight of this lens compares favorably with the existing wearable night vision optics.

D. Medium Scale Lens ($f = 112$ mm, F/2.33, 486–656 nm)

A 10GPix monocentric multiscale imager prototype was designed and built for the AWARE program

Table 12. Optical Prescription of the Short-Wave Infrared Monocentric Lens

	Radius	Thickness	Glass	Semi-Diameter
OBJ	Infinity	Infinity		Infinity
1	9.64853	6.08158	M-FDS2	9.22685
2	3.56695	3.56695	K-GIR79	3.55045
STO	Infinity	3.56695	K-GIR79	2.81170
4	-3.56695	2.13160	K-PSFN215	3.52510
5	-5.69855	0.20974		5.40924
6	-5.90829	4.27312	N-SF4	5.56372
7	-10.18141	1.79011		9.05080
IMA	-11.97152			10.36887

[31]. The system was a 2GS monocentric objective lens of F2 and S-BSL7 glass, designed to work in combination with the secondary relay optics. While the objective lens itself was not diffraction limited (with RMS spot size 11 times larger than the Airy disc) the whole system was designed to be diffraction-limited. We identified better stand-alone objective designs in the 2GS and 3GS architecture, but these lenses are not easily fabricated due to size limitations of available glass slabs. Size restrictions may provide a hard constraint on the materials choice for the outer shells in large monocentric lenses.

Under this constraint, the 4GA-8 monocentric architecture was unable to achieve a diffraction limited $f = 112$ mm objective, so we used a 5GA-10 architecture, choosing N-BK7 and F2 glasses for the outer shells as they can be melted in blanks up to 500 mm thick [36]. Such lenses are more expensive to fabricate than the two-glass objective, but they are compatible with fiber-optic image transfer. Prescription of the lens is shown in Table 13, and layout with MTF performance in Fig. 23. Similar designs can be obtained using Ohara S-FPM2 glass instead of Sumita K-GFK68 glass for the core material.

E. Large Scale Lens ($f = 280$ mm, F/2.8, 450–700 nm)

In 2010, Brady and Marks [19] presented a 5GA-10 architecture monocentric lens design capable of up to 40 Gigapixels overall resolution. In the journal publication that followed [37], the group used a statistical approach to conduct a global search for this lens using the Schott glass catalog and a specific merit function. We performed our search using the merit function of our 5D near-global optimizer using the same pool of glasses (Schott catalog, as of October 2010) and obtained the 4GA-8 geometry solution shown in Fig. 24 and Table 14.

Table 13. Optical Prescription of the $f = 112$ mm Monocentric Lens Candidate

	Radius	Thickness	Glass	Semi-Diameter
OBJ	Infinity	Infinity		Infinity
1	70.6495	25.0385	F2	66.0262
2	45.6110	20.0201	N-LASF31A	43.4394
3	25.5910	25.5910	K-GFK68	25.0475
STO	Infinity	25.5910	K-GFK68	15.0900
5	-25.5910	11.0541	N-LASF31A	24.8256
6	-36.6451	5.7785		34.6924
7	-42.4236	34.4507	N-BK7	39.4128
8	-76.8743	35.0734		68.5323
IMA	-111.9476			96.9500

Table 14. Optical Prescription of the Optimal 40GPix Monocentric 4GA-8 Lens

	Radius	Thickness	Glass	Semi-Diameter
OBJ	Infinity	Infinity		Infinity
1	122.6509	65.5070	N-LAK33B	116.1051
2	57.1440	57.1440	CAF2	56.0001
STO	Infinity	57.1440	CAF2	34.8902
4	-57.1440	16.2656	N-LAK8	55.6673
5	-73.4095	11.4827		70.3637
6	-84.8922	31.3242	N-LAF34	80.0069
7	-116.2164	163.6565		107.5578
IMA	-279.8730			242.3780

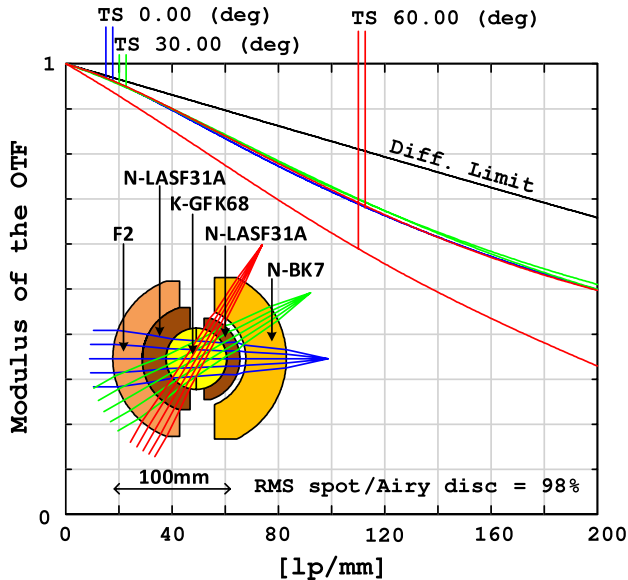


Fig. 23. Medium scale monocentric lens 5GA-10 diffraction limited candidate possible to fabricate (112 mm focal length, $F/2.33$, 486–656 nm).

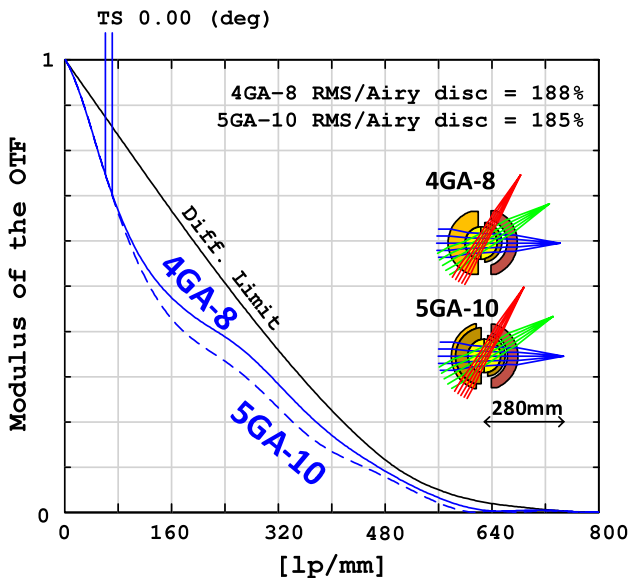


Fig. 24. Polychromatic MTF comparison of previously reported 5GA-10 optimal solution for the Gigagon 40GPix lens and a simpler 4GA-8 solution (280 mm focal length, $F/2.8$, 450–700 nm).

The resulting 4GA-8 lens offers comparable size and weight, and slightly better MTF performance, than the 5GA-10 lens. It is necessary to note, however, that both lenses would be difficult to fabricate due to the physical thickness of the glass elements required.

6. Summary and Conclusion

This paper describes an investigation of wide field of view monocentric lenses using architectures with complexity ranging from a simple glass ball to moderately complex structures with up to 10 degrees of design freedom following the focal length constraint. A 2GS lens structure works well for applications with a moderate spectral range, focal length, and numerical aperture. However, for applications that substantially increase one or more of these specifications, we show that the best performance in a moderate complexity lens is achieved with four-glass structures with an air gap between meniscus elements behind a spherical glass core (the 4GA-8 architecture).

To help identify the best specific designs for such 4GA-8 lenses, we presented a systematic optimization method derived from the global optimization of a two-glass lens and demonstrate its capability for several case studies. We conclude that the general class of monocentric objective lenses offers practical high-performance options for a variety of wide-angle imaging systems.

This research was supported by the DARPA SCE-NICC program under contract W911NF-11-C-0210 and by the DARPA AWARE program under contract HR0011-10C-0073.

References

1. D. J. Brady, M. E. Gehm, R. A. Stack, D. L. Marks, D. S. Kittle, D. R. Golish, E. M. Vera, and S. D. Feller, "Multiscale gigapixel photography," *Nature* **486**, 386–389 (2012).
2. J. E. Ford and E. Tremblay, "Extreme form factor imagers," in *Imaging Systems*, OSA Technical Digest (CD) (Optical Society of America, 2010), paper IMC2.
3. E. J. Tremblay, D. L. Marks, D. J. Brady, and J. E. Ford, "Design and scaling of monocentric multiscale imagers," *Appl. Opt.* **51**, 4691–4702 (2012).
4. J. A. Waidelich, Jr., "Spherical lens imaging device," U.S. patent 3,166,623 (19 January 1965).
5. T. S. Axelrod, N. J. Colella, and A. G. Ledebuhr, "The wide-field-of-view camera," in *Energy and Technology Review*, (Lawrence Livermore National Laboratory, 1988).

6. C. Akerlof, M. Fatuzzo, B. Lee, R. Bionta, A. Ledebuhr, H. Park, S. Barthelmy, T. Cline, and N. Gehrels, "Gamma-ray optical counterpart search experiment (GROCSE)," in *AIP Conference Proceedings* (American Institute of Physics, 1994), Vol. **307**, pp. 633–637.
7. J. F. Kordas, I. T. Lewis, B. A. Wilson, D. P. Nielsen, H. Park, R. E. Priest, R. Hills, M. J. Shannon, A. G. Ledebuhr, and L. D. Pleasance, "Star tracker stellar compass for the Clementine mission," *Proc. SPIE* **2466**, 70 (1995).
8. I. Stamenov, I. Agurok, and J. Ford, "Optimization of two-glass monocentric lenses for compact panoramic imagers: general aberration analysis and specific designs," *Appl. Opt.* **51**, 7648–7661 (2012).
9. J. Ford, I. Stamenov, S. Olivas, G. Schuster, N. Motamedi, I. Agurok, R. Stack, A. Johnson, and R. Morrison, "Fiber-coupled monocentric lens imaging," in *Imaging and Applied Optics*, J. Christou and D. Miller, eds. OSA Technical Digest (online) (Optical Society of America, 2013), paper CW4C.2.
10. W. Smith, *Modern Lens Design*, 2nd ed. (McGraw-Hill, 2005).
11. J. M. Cobb, D. Kessler, and J. Agostinelli, "Optical design of a monocentric autostereoscopic immersive display," *Proc. SPIE* **4832**, 80–90 (2002).
12. G. Krishnan and S. K. Nayar, "Towards a true spherical camera," *Proc. SPIE* **7240**, 724002 (2009).
13. O. Cossairt, D. Miao, and S. K. Nayar, "Gigapixel computational imaging," in *IEEE International Conference on Computational Photography* (IEEE, 2011).
14. R. Kingslake, *A History of the Photographic Lens* (Academic, 1989), pp. 49–67.
15. H. Son, D. L. Marks, E. J. Tremblay, J. Ford, J. Hahn, R. Stack, A. Johnson, P. McLaughlin, J. Shaw, J. Kim, and D. J. Brady, "A multiscale, wide field, gigapixel camera," in *Imaging Systems Applications*, OSA Technical Digest (Optical Society of America, 2011), paper JTUE2.
16. J. Oakley, "Whole-angle spherical retroreflector using concentric layers of homogeneous optical media," *Appl. Opt.* **46**, 1026–1031 (2007).
17. M. Born and E. Wolf, *Principles of Optics* 7th ed. (Cambridge University, 1999).
18. I. Stamenov, I. Agurok, and J. Ford, "Capabilities of monocentric objective lenses," in *Imaging and Applied Optics*, J. Christou and D. Miller, eds. OSA Technical Digest (online) (Optical Society of America, 2013), paper ITu3E.4.
19. D. Marks and D. Brady, "Gigagon: a monocentric lens design imaging 40 gigapixels," in *Imaging System* OSA Technical Digest (CD) (Optical Society of America, 2010).
20. R. Kingslake and R. B. Johnson, *Lens Design Fundamentals*, 2nd ed. (SPIE, 2010).
21. G. G. Slyusarev, *Aberrations and Optical Design Theory*, 2nd ed. (Adam Hilger, 1984).
22. M. M. Rusinov, *Handbook of Computational Optics* (Mashinostroenie, 1984), Chap. 23.
23. P. Gill, W. Murray, and M. Wright, *Practical Optimization* (Academic, 1981).
24. S. A. Rodionov, *Computer Lens Design* (Mashinostroenie, 1982).
25. D. Feder, "Automatic optical design," *Appl. Opt.* **2**, 1209–1226 (1963).
26. G. Golub and C. Van Loan, *Matrix Computations* (John Hopkins, 1989).
27. R. Shannon, *The Art and Science of Optical Design* (Cambridge University, 1997).
28. <http://www.andor.com/learning-academy/ccd-spectral-response-qe-defining-the-qe-of-a-ccd>.
29. M. Kruger, B. Panov, B. Kulagin, G. Pogarev, Y. Kruger, and A. Levinson, "Handbook of opto-mechanics," Moscow, 1963.
30. www.norlandprod.com.
31. D. L. Marks, H. S. Son, J. Kim, and D. Brady, "Engineering a gigapixel monocentric multiscale camera," *Opt. Eng.* **51**, 083202 (2012).
32. M. Rusinov, *Composition of Optical Systems* (Mashinostroenie, 1989).
33. www.morovision.com.
34. D. Dayton, J. Gonglewsky, C. Arnauld, I. Mons, and D. Burns, *SWIR Sky Glow Cloud Correlation with NIR and Visible Clouds: An Urban and Rural Comparison* (AFRL, 2009).
35. www.sensorsinc.com.
36. www.schott.com, TIE-41 Large Optical Glass Blanks, Technical information document.
37. N. Zheng, S. C. Schmidler, D. Marks, and D. Brady, "Computer experiment and global optimization of layered monocentric lens systems," *Optik* **123**, 1249–1259 (2012).